



# In situ constructing interfacial contact $\text{MoS}_2/\text{ZnIn}_2\text{S}_4$ heterostructure for enhancing solar photocatalytic hydrogen evolution

Zizhong Zhang\*, Lin Huang, Jiangjie Zhang, Fengjiao Wang, Yanyu Xie, Xiaotong Shang, Yuyao Gu, Huibo Zhao, Xuxu Wang

State Key Laboratory of Photocatalysis on Energy and Environment, Research Institute of Photocatalysis, College of Chemistry, Fuzhou University, PR China

## ARTICLE INFO

### Keywords:

Photocatalysis  
 $\text{MoS}_2/\text{ZnIn}_2\text{S}_4$   
 Heterostructure  
 $\text{H}_2$  evolution

## ABSTRACT

Construction of heterostructure by intimately interfacing two or more semiconductor materials with different geometrical and electronically energetic alignments at nanoscale is very important to achieve the composite photocatalysts with a high photocatalytic efficiency. Here, we in-situ prepared an intimate contact  $\text{MoS}_2/\text{ZnIn}_2\text{S}_4$  heterostructure photocatalyst by a one-pot solvothermal reaction. The  $\text{MoS}_2/\text{ZnIn}_2\text{S}_4$  heterostructure significantly enhanced the photocatalytic  $\text{H}_2$  evolution of  $\text{ZnIn}_2\text{S}_4$  under visible light illumination. The hydrogen evolution rate reaches  $3891.6 \mu\text{mol g}^{-1} \text{h}^{-1}$  over 5%- $\text{MoS}_2/\text{ZnIn}_2\text{S}_4$ , which exceeded the photocatalytic activity of Pt-loaded  $\text{ZnIn}_2\text{S}_4$  samples. The subtle atomic-level intimate contact and strong interactions between  $\text{ZnIn}_2\text{S}_4$  and  $\text{MoS}_2$  was ascribed to a highly efficient charge carrier separation and thus photocatalytic activity for  $\text{MoS}_2/\text{ZnIn}_2\text{S}_4$ . These results provide inspiration for the design of composited photocatalysts with efficient photocatalytic  $\text{H}_2$  evolution.

## 1. Introduction

Photocatalytic hydrogen evolution from water has attracted the interest of many researchers as a green energy and sustainable technology [1]. Great efforts have been devoted to the development of highly efficient semiconductor photocatalysts for  $\text{H}_2$  production. Up to date, catalytic materials have been developed from the original  $\text{TiO}_2$  to various new photocatalysts, including MOFs [2–4], COFs [5–7],  $\text{C}_3\text{N}_4$  [8–11],  $\text{Ta}_3\text{N}_5$  [12],  $\text{TaON}$  [13],  $\text{CdS}$  [14–17] and all kinds of composite catalysts such as  $\text{Cd}_{0.5}\text{Zn}_{0.5}\text{S}$  QDs@ $\text{C}_3\text{N}_4$  [18],  $\text{Co}_2\text{P@Co}_3\text{O}_4$  [19],  $\text{CdZnS@LDH}$  [20]. And the wavelength response range of photocatalyst was extended from UV to visible light [21,22], even far infrared. However, the photocatalytic  $\text{H}_2$  production still suffers from low conversion efficiencies, resulting from the fast electron-hole recombination rate in the photocatalysts. So searching for excellent semiconductor materials and improving the photocatalytic efficiency of light absorption have become a pressing matter of the moment.

To improve the efficiency of the photocatalytic  $\text{H}_2$  evolution, an ideal photocatalyst should possess: (1) a narrow band gap to allow for efficient absorption of solar energy; (2) a highly efficient charge spatial separation; (3) the level of the conduction band (CB) and the valence band (VB) for accumulating the photoexcited electrons and holes with a large enough potential in both the thermodynamics and the kinetics to achieve redox  $\text{H}_2\text{O}$  reaction. Many metal chalcogenides, such as  $\text{CdS}$ ,

$\text{In}_2\text{S}_3$ ,  $\text{Bi}_2\text{S}_3$ , and  $\text{CuS}$  being narrow band gaps with strong absorption in the visible light region, have been demonstrated as good candidates for photocatalytic water splitting to produce hydrogen in the presence of sacrificial reagents [23–26]. Thus, in many of the newly designed and constructed photocatalytic reaction based on semiconductors, the hydrogen production performance of metal sulfides is particularly prominent. Unfortunately, the metal sulfide also has a fatal disadvantage in the light of the photocatalytic reaction, such as fast recombination of electron-hole pairs and serious light corrosion under light illumination. Recent studies have demonstrated that introducing heteroatom/second component into/onto metal chalcogenides to construct multi-component sulphides is one of the compelling ways to further tune their properties and optimize their performance for photocatalytic hydrogen production. Among these, as the only member of  $\text{AB}_2\text{X}_4$  ( $\text{A} = \text{Cu, Ag, Zn, Cd, etc.}$ ;  $\text{B} = \text{Al, Ga, In}$ ;  $\text{X} = \text{S, Se, Te}$ ) family semiconductors with a layered structure, ternary sulfide  $\text{ZnIn}_2\text{S}_4$  is a n-type semiconductor with a bandgap of 2.4 eV, along with considerable photo- and chemical stability, which has attracted considerable attentions for the possible application in photocatalytic hydrogen production [27–30]. However, it should be noted that the photocatalytic activity of  $\text{ZnIn}_2\text{S}_4$  still needed to be further improved.

Construction of heterostructure by intimately interfacing two or more semiconductor materials with different geometrical and electronically energetic alignments at nanoscale is the most popular strategy to

\* Corresponding author.

E-mail address: [z.zhang@fzu.edu.cn](mailto:z.zhang@fzu.edu.cn) (Z. Zhang).

achieve the composite photocatalysts with a high photocatalytic efficiency [26,31,32], but still remains very challenge. To maximize the efficiency of  $\text{ZnIn}_2\text{S}_4$  through enhancing the effective separation and transfer of photoinduced electrons and holes, the incorporated composites should have several properties including: (1) the conduction band and valence band positions of composites must well match with the corresponding band of  $\text{ZnIn}_2\text{S}_4$  to directionally migrate the photo-generated charges driven by the built-in electric field existing in the contact interface; (2) Similar properties with  $\text{ZnIn}_2\text{S}_4$  is beneficial to tightly attached to  $\text{ZnIn}_2\text{S}_4$  and strengthen the interaction between them; (3) The composite has an increased interface contact area for photogenerated charge transfer. Recent studies have demonstrated that the  $\text{ZnIn}_2\text{S}_4$  nanomaterials was selectively coupled with other semiconductors ( $\text{TiO}_2$ ,  $\text{CdS}$ ,  $\text{ZnS}$ ,  $\text{MoS}_2$ ,  $\text{NiS}$ , and so on) or carbon-based materials or noble metals (e.g., Pt) to enhance the charge separation and photocatalytic hydrogen-production activities [33–39].

$\text{MoS}_2$  is a typical TMDs- transition metal dichalcogenides [40] and has a sandwiched layered structure consisting of Mo atoms layer between two hexagonally arranged S atoms layers [41]. The hexagonal  $\text{ZnIn}_2\text{S}_4$  also has a sandwiched layered structure which are based on a stacking of packets of S-Zn-S-In-S-In-S atoms layers [42]. It is expected that it is facile to grow layer  $\text{MoS}_2$  on hexagonal  $\text{ZnIn}_2\text{S}_4$  surface to form the intimate 2D nanojunction with an increased contact surface area in accelerating the charge transfer. Besides this, due to their analogous sulfides,  $\text{MoS}_2$  is beneficial to tightly bound to  $\text{ZnIn}_2\text{S}_4$  by minimizing the lattice mismatch and strengthen the interaction between them. Moreover, the conduction band position of  $\text{MoS}_2$  (−0.5 to −0.9 eV vs. NHE) is less negative as compared to that of hexagonal  $\text{ZnIn}_2\text{S}_4$  (−1.1 eV vs. NHE) and thus provides possibility for a directional transfer of the photo-generated electrons from  $\text{ZnIn}_2\text{S}_4$  to  $\text{MoS}_2$ . Therefore, it is supposed that  $\text{MoS}_2$  can be an ideal incorporated composite for hexagonal  $\text{ZnIn}_2\text{S}_4$  in photocatalytic  $\text{H}_2$  evolution.

In this work, we in-situ constructed a highly efficient  $\text{MoS}_2/\text{ZnIn}_2\text{S}_4$  photocatalyst by a very simple one-pot solvothermal method, which endows the subtle atomic-level intimate contact between  $\text{MoS}_2$  and  $\text{ZnIn}_2\text{S}_4$ . The  $\text{MoS}_2/\text{ZnIn}_2\text{S}_4$  composites displayed an uniform hierarchical microsphere morphology. As a result, the fabricated  $\text{MoS}_2/\text{ZnIn}_2\text{S}_4$  composited photocatalysts exhibit a high  $\text{H}_2$  evolution rate in the presence of  $\text{Na}_2\text{S}/\text{Na}_2\text{SO}_3$  as sacrificial agents under visible light irradiation. The prepared  $\text{MoS}_2/\text{ZnIn}_2\text{S}_4$  heterostructures display a better photocatalytic activity of hydrogen evolution as compared with the reported  $\text{MoS}_2/\text{ZnIn}_2\text{S}_4$  heterostructure photocatalyst synthesized through conventional methods under the similar conditions [42,43–46]. This work provides inspiration for the design of the intimate contact heterostructure photocatalysts with efficient photocatalytic  $\text{H}_2$  evolution.

## 2. Experimental section

### 2.1. Materials

Zinc chloride ( $\text{ZnCl}_2$ ), indium chloride ( $\text{InCl}_3 \cdot 4\text{H}_2\text{O}$ ), sodium molybdate dehydrate ( $\text{Na}_2\text{MoO}_4 \cdot 2\text{H}_2\text{O}$ ), thiocetamide (TAA), ethanol (ET) were obtained from sinopham chemical Reagent Co., Ltd (Shanghai, China). All materials were used as received without further purification. Deionized water used was obtained from local sources.

### 2.2. Photocatalyst preparation

The x%- $\text{MoS}_2/\text{ZnIn}_2\text{S}_4$  samples were prepared following a previous reported literature with a slight modification [47]. Typically, the certain sodium molybdate dehydrate ( $\text{Na}_2\text{MoO}_4 \cdot 2\text{H}_2\text{O}$ ),  $\text{ZnCl}_2$  (1 mmol), and  $\text{InCl}_3 \cdot 4\text{H}_2\text{O}$  (2 mmol) were added into 27 mL alcohol with vigorously stirring for 0.5 h to obtain the homogeneous solution. And then the excessive TAA (8 mmol) was dispersed in the mixture solution, which was going on vigorously stirring for 0.5 h. Finally, the mixture

solutions were transferred into 100 mL Teflon-lined stainless steel autoclave and kept at 433 K for 24 h. The final products were gradually cooled to room temperature and then repeatedly washed several times with deionized water and ethanol by centrifugation and were dried at 333 K using the vacuum oven for overnight. The molar ratios of  $\text{MoS}_2$  to  $\text{ZnIn}_2\text{S}_4$  were controlled to be 1%, 3%, 5%, 8%, 10%, and the synthesized samples were labeled as 1%-MS/ZIS, 3%-MS/ZIS, 5%-MS/ZIS, 8%-MS/ZIS, 10%-MS/ZIS. The pure  $\text{ZnIn}_2\text{S}_4$  was synthesized through the above steps without sodium molybdate dehydrate ( $\text{Na}_2\text{MoO}_4 \cdot 2\text{H}_2\text{O}$ ), and also was marked as ZIS.

### 2.3. Characterization

The (Bruker D8 Advance) X-ray diffraction (XRD) using  $\text{Cu K}\alpha_1$  radiation ( $\lambda = 0.15418 \text{ nm}$ ) was applied to characterize the crystal phase properties of as-prepared products. The field emission scanning electron microscopy (FE-SEM) (Hitachi New Generation SU8010) was used to characterize the morphology of the samples. The detailed microstructure of the samples was measured by Transmission electron microscope and High-resolution transmission electron microscope (TEM) (JEOL-2010). Nitrogen adsorption-desorption isotherms (BET) were collected on a Micromeritics ASAP2020 analyzer. The X-ray photoelectron spectroscopy (XPS) analysis was conducted on ESCALAB 250 photoelectron spectroscope (Thermo Fisher Scientific) with monochromatic  $\text{Al K}\alpha$  radiation (200 W). The optical absorption of samples was gotten by UV-vis spectrophotometer (Cary 500, Varian Co.), in which  $\text{BaSO}_4$  was used as the internal reflectance standard. The Edinburgh FL/FS900 spectrophotometer was used to obtain the photoluminescence spectra (PL) for products under  $\lambda > 420 \text{ nm}$  irradiation source.

### 2.4. Photocatalytic reaction test

$\text{H}_2$  evolution reactions were carried out in a closed gas-circulation system (Perfectlight, Beijing). In this system, 80 mg catalyst was dispersed in 100 mL aqueous solution containing 0.35 M  $\text{Na}_2\text{S}$  and 0.25 M  $\text{Na}_2\text{SO}_3$  as sacrificial agents and continuously stirred until the end of the reaction. After removing air from the reaction system, the solution was irradiated by a 300 W xenon lamp equipped with a  $\lambda > 420 \text{ nm}$  cut-off filter. At the same time, the reaction was still maintained at  $5^\circ\text{C}$  with a circulating condensate system. Finally, the amount of  $\text{H}_2$  product was measured by gas chromatography (GA-80) with a thermal conductive detector (TCD).

## 3. Results and discussion

### 3.1. Characterization of $\text{MoS}_2/\text{ZnIn}_2\text{S}_4$ photocatalysts

The crystallinity phase of the as-prepared  $\text{ZnIn}_2\text{S}_4$  and  $\text{MoS}_2/\text{ZnIn}_2\text{S}_4$  composites were investigated by power X-ray diffraction (XRD) pattern. As shown in Fig. 1, the parent  $\text{ZnIn}_2\text{S}_4$  displayed six main peaks at  $2\theta$  degrees of 21.48, 27.90, 39.45, 47.24, 51.95, 55.85°, which can be well indexed to (006), (102), (108), (112), (1012) and (202) reflections of the hexagonal  $\text{ZnIn}_2\text{S}_4$  (JCPDS card No. 03-065-2023), respectively. As compared, the  $\text{MoS}_2/\text{ZnIn}_2\text{S}_4$  composites had the similar XRD patterns with the parent  $\text{ZnIn}_2\text{S}_4$  and no diffraction peaks corresponding to  $\text{MoS}_2$  can be observed. This may be due to the less content of  $\text{MoS}_2$  or the excessively weak response of  $\text{MoS}_2$  compared with those of  $\text{ZnIn}_2\text{S}_4$  so that it was not detected in the XRD diffraction. Moreover, the intensity and width of XRD peaks of  $\text{ZnIn}_2\text{S}_4$  was independent of  $\text{MoS}_2$  hybrid. This indicates that the  $\text{MoS}_2$  hybrid has almost no influence on the crystallinity and the particle size of  $\text{ZnIn}_2\text{S}_4$ .

The morphologies of the prepared samples were observed by the field emission scanning electron microscopic (FESEM). Fig. 2 clearly showed that the as-prepared  $\text{ZnIn}_2\text{S}_4$  exhibited a flower-like microspheres assembled by the nanosheets. Furthermore, the hierarchical

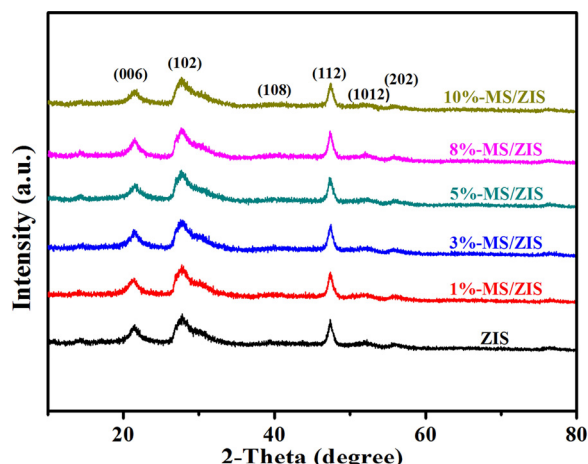


Fig. 1. XRD pattern of the parent  $\text{ZnIn}_2\text{S}_4$  and  $\text{MoS}_2/\text{ZnIn}_2\text{S}_4$  composites.

microspheres had a nearly uniform size distribution in the range of 4–6  $\mu\text{m}$  with the thickness of the nanosheet being 20–50 nm. The different molar ratio of  $\text{MoS}_2$  hybrid had almost no change in the morphology of  $\text{ZnIn}_2\text{S}_4$ . The hierarchical microsphere morphologies of the  $\text{MoS}_2/\text{ZnIn}_2\text{S}_4$  composites could lead to a high specific surface and plenty of microspore structure, which are advantageous to the reactant adsorption and mass transfer, and thus results in a high photocatalytic activity.

The more detailed microstructures of  $\text{MoS}_2/\text{ZnIn}_2\text{S}_4$  hybrid were furthermore investigated by transmission electron microscopy (TEM) and high resolution transmission electron microscopy (HRTEM). In the Fig. 3a, the gauze-like edge of the nanoflower was clearly observed to further verify that the synthetic  $\text{MoS}_2/\text{ZnIn}_2\text{S}_4$  hybrids were stacked and self-assembled through thin nanoplates. However, the  $\text{ZnIn}_2\text{S}_4$  and  $\text{MoS}_2$  could not be distinguished in TEM images, which may be due to the co-growth of  $\text{ZnIn}_2\text{S}_4$  and  $\text{MoS}_2$  nanoplates to be intertwined and closely knit together during the synthesis of composite samples. Fig. 3b clearly showed that the composite was made up of  $\text{ZnIn}_2\text{S}_4$  and  $\text{MoS}_2$  and they were tightly combined with each other to form closely hybrid

structure. The two different inter-planar spacing ( $d$ ) were observed to be 0.32 nm and 0.63 nm, which can be assigned to the (102) planes of hexagonal  $\text{ZnIn}_2\text{S}_4$  and (002) planes of hexagonal  $\text{MoS}_2$ , the intersecting lattice stripes strongly verified the subtle atomic-level intimate contact interface. The Mo, In, Zn, and S elements were detected in the corresponding EDX elemental mappings (Fig. 3c) and these elements were evenly distributed in the tested area. The above results fully proved that one-pot solvothermal reaction could successfully synthesize  $\text{MoS}_2/\text{ZnIn}_2\text{S}_4$  composite, and the intimate contact was well formed that is beneficial to transfer the photogenerated charge carriers between  $\text{ZnIn}_2\text{S}_4$  and  $\text{MoS}_2$ , which could be a key factor in determining the very good photocatalytic  $\text{H}_2$  production activity.

The BET surface area and pore structure of the pure  $\text{ZnIn}_2\text{S}_4$  and 5%- $\text{MoS}_2/\text{ZnIn}_2\text{S}_4$  samples were investigated by  $\text{N}_2$  adsorption-desorption measurement, as shown in Figs. 4, S1 and Table. S1. The curve shape of the samples belonged to type IV isotherm with hysteresis loops characteristic of mesoporous structure. The BET surface area was increased from 12.3 to 34.7  $\text{m}^2\text{g}^{-1}$  with increasing  $\text{MoS}_2$  up to 5%. However, when the molar ratio of theoretically  $\text{MoS}_2$  exceeded 5%, the BET surface area of the synthesized composite samples had almost no change. This was because the formation of  $\text{ZnIn}_2\text{S}_4$  and  $\text{MoS}_2$  could be competed with each other in the synthesis process of one-pot solvothermal reaction. The formation and stacking of  $\text{ZnIn}_2\text{S}_4$  nanosheets were hindered by  $\text{MoS}_2$  composites, so that the composite  $\text{MoS}_2/\text{ZnIn}_2\text{S}_4$  nanoflowers stacked more loosely than the pure  $\text{ZnIn}_2\text{S}_4$ . This is consistent with the change in flower-like microsphere morphology of  $\text{MoS}_2/\text{ZnIn}_2\text{S}_4$  composite in SEM images. The larger surface area of composite samples may expose more activity sites, which improve the photocatalytic activity. The composited  $\text{MoS}_2$  had no significant effect on the pore diameter of the prepared samples in the range of 1.5–3.1 nm.

The influence of the introduction of  $\text{MoS}_2$  on the surface chemical states of  $\text{ZnIn}_2\text{S}_4$  was investigated by X-ray photoelectron spectroscopy (XPS) characterization. As shown in Fig. 5a, for pure  $\text{ZnIn}_2\text{S}_4$ , the XPS peaks of the Zn  $2p_{3/2}$  and Zn  $2p_{1/2}$  was located respectively at 1023.3 and 1046.3 eV, which is consistent with many reported  $\text{ZnIn}_2\text{S}_4$  samples [40]. When  $\text{MoS}_2$  was composited with  $\text{ZnIn}_2\text{S}_4$ , the binding energy of Zn 2p peaks were positively shifted to a higher value with increasing  $\text{MoS}_2$  contents. The XPS peaks of the Zn  $2p_{3/2}$  was shifted to 1023.6 eV

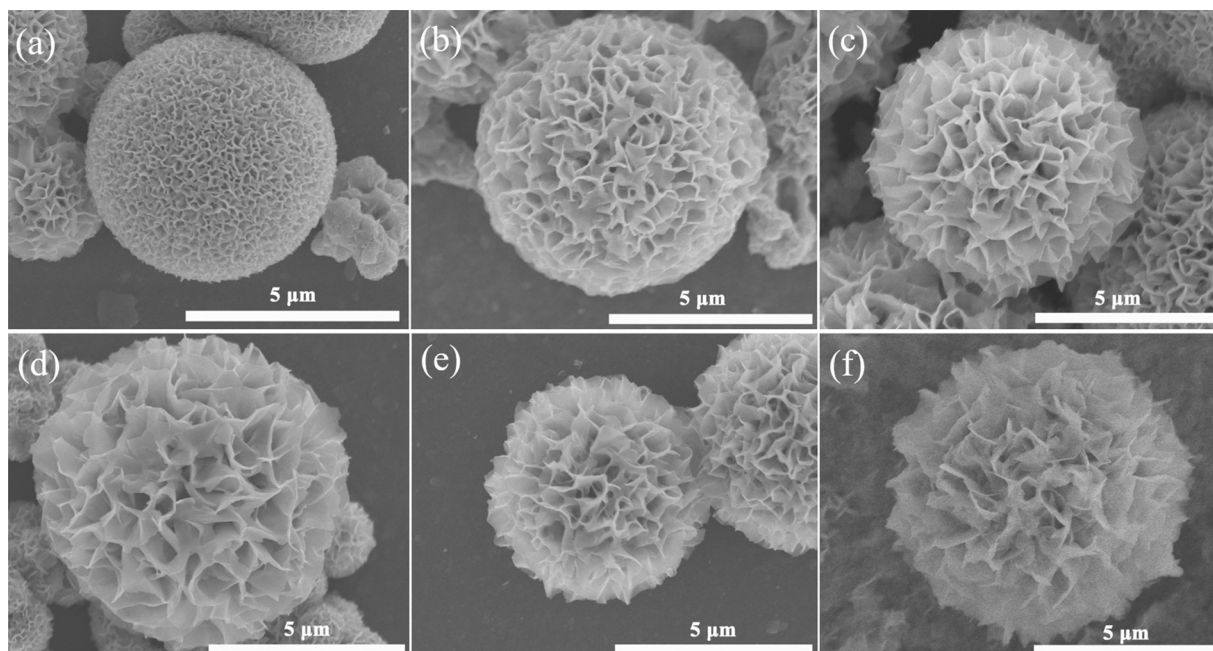


Fig. 2. SEM images of the  $\text{ZnIn}_2\text{S}_4$  (a) and 1%- $\text{MoS}_2/\text{ZnIn}_2\text{S}_4$  (b) and 3%- $\text{MoS}_2/\text{ZnIn}_2\text{S}_4$  (c) and 5%- $\text{MoS}_2/\text{ZnIn}_2\text{S}_4$  (d) and 8%- $\text{MoS}_2/\text{ZnIn}_2\text{S}_4$  (e) and 10%- $\text{MoS}_2/\text{ZnIn}_2\text{S}_4$  (f).



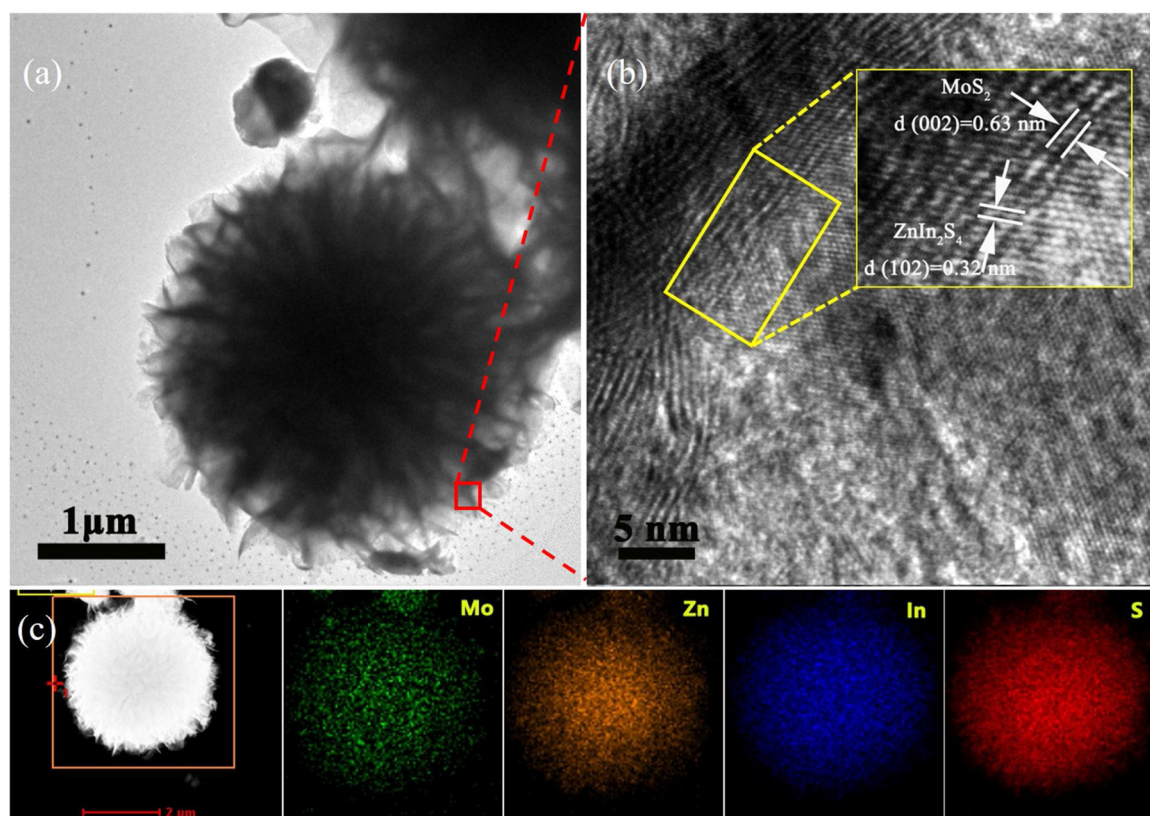


Fig. 3. TEM image (a); HRTEM image corresponding to the red frames (b); corresponding EDX elemental mapping of Mo, Zn, In, and S of the MoS<sub>2</sub>/ZnIn<sub>2</sub>S<sub>4</sub> (c).

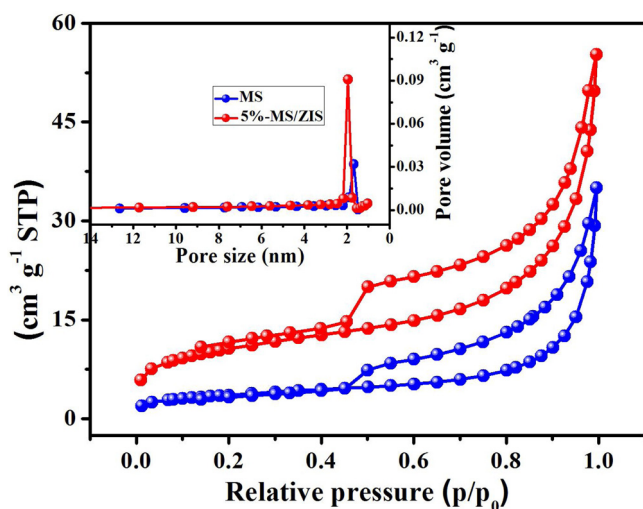


Fig. 4. N<sub>2</sub> adsorption-desorption isotherms of ZnIn<sub>2</sub>S<sub>4</sub> and 5%-MoS<sub>2</sub>/ZnIn<sub>2</sub>S<sub>4</sub>, the inset is the Barrett-Joyner-Halenda (BJH) pore size distribution curve.

by a 0.3 eV for the 8%-MoS<sub>2</sub>/ZnIn<sub>2</sub>S<sub>4</sub> as compared with the parent ZnIn<sub>2</sub>S<sub>4</sub>. In Fig. 5b, the XPS peaks at 445.2 and 52.8 eV were attributed to the In 3d<sub>5/2</sub> and In 3d<sub>3/2</sub> for pure ZnIn<sub>2</sub>S<sub>4</sub>. MoS<sub>2</sub> hybrid also led to a positive shift in the binding energy of In 3d to a higher value with increasing MoS<sub>2</sub> contents. These confirmed that a strong interaction was formed between ZnIn<sub>2</sub>S<sub>4</sub> and MoS<sub>2</sub>, and thus facilitated the electron transfer from ZnIn<sub>2</sub>S<sub>4</sub> to MoS<sub>2</sub> resulting in the shift of binding energy of Zn 2p and In 3d in ZnIn<sub>2</sub>S<sub>4</sub> to the higher value. The S 2p spectra (Fig. 5c) were fitted into S 2p<sub>1/2</sub> and S 2p<sub>3/2</sub> peaks respectively at 161.37 and 162.51 eV for pure ZnIn<sub>2</sub>S<sub>4</sub>. With the increase of MoS<sub>2</sub> loading, the XPS peaks of S 2p were obviously shifted to higher binding energy, which is due to the fact that the transfer of electrons from

ZnIn<sub>2</sub>S<sub>4</sub> to MoS<sub>2</sub> was facilitated at the two-phase interface by MoS<sub>2</sub> loading. On the contrary, the Mo 3d<sub>3/2</sub> binding energy was gradually decreased with increasing MoS<sub>2</sub> contents, as shown in Fig. 5d. This also verified the charge transfer direction from ZnIn<sub>2</sub>S<sub>4</sub> to MoS<sub>2</sub> in MoS<sub>2</sub>/ZnIn<sub>2</sub>S<sub>4</sub> composites.

The optical absorption properties of the samples were measured by the UV-vis diffuse reflectance spectroscopy (DRS), as shown in Fig. 6. The parent ZnIn<sub>2</sub>S<sub>4</sub> had a wide absorption in visible region with a steep absorption edge at about 490 nm, indicating that the UV-vis absorption of ZnIn<sub>2</sub>S<sub>4</sub> can be due to the band gap transition but not the transition from impurity levels to the conduction band. Because the pure MoS<sub>2</sub> could be fully absorbed in the entire UV-vis region at a range of 200–800 nm, the combination together of MoS<sub>2</sub> and ZnIn<sub>2</sub>S<sub>4</sub> led to an increase in the visible-light absorption of the composite samples. A heterostructure was formed between ZnIn<sub>2</sub>S<sub>4</sub> and MoS<sub>2</sub> in the prepared MoS<sub>2</sub>/ZnIn<sub>2</sub>S<sub>4</sub> composites to narrow the band gap of ZnIn<sub>2</sub>S<sub>4</sub>, and thus a red shift of the light absorption of the composite samples. The larger red shift appeared with the more content of MoS<sub>2</sub> loading [44,48]. This is well consistent with the color change from bright yellow to dark brown of the samples. Obviously, the introduction of MoS<sub>2</sub> can make ZnIn<sub>2</sub>S<sub>4</sub> more effective utilization of solar energy.

In order to investigate the enhanced efficiency of separation and transfer of photogenerated carriers by MoS<sub>2</sub> hybrid, the transient photocurrent response of the pristine ZnIn<sub>2</sub>S<sub>4</sub> and 5%-MoS<sub>2</sub>/ZnIn<sub>2</sub>S<sub>4</sub> composite was compared under visible light irradiation by a 300 W Xe lamp equipped with a  $\lambda > 420$  nm cutoff filter. As can be seen in Fig. 7a, the photocurrent density of the pure ZnIn<sub>2</sub>S<sub>4</sub> of 6.03  $\mu\text{A cm}^{-2}$  was relatively low compared to that of 5%-MoS<sub>2</sub>/ZnIn<sub>2</sub>S<sub>4</sub> of 8.43  $\mu\text{A cm}^{-2}$ . The results confirmed that MoS<sub>2</sub> can improve the separation efficiency of photogenerated electrons and holes pairs of ZnIn<sub>2</sub>S<sub>4</sub>, which can contribute to the electron transfer from ZnIn<sub>2</sub>S<sub>4</sub> to MoS<sub>2</sub>. In order to further detect the photon utilization of the synthesized samples under visible light, the incident photon-to-electron conversion efficiency (IPCE) was performed for the pure ZnIn<sub>2</sub>S<sub>4</sub> and the

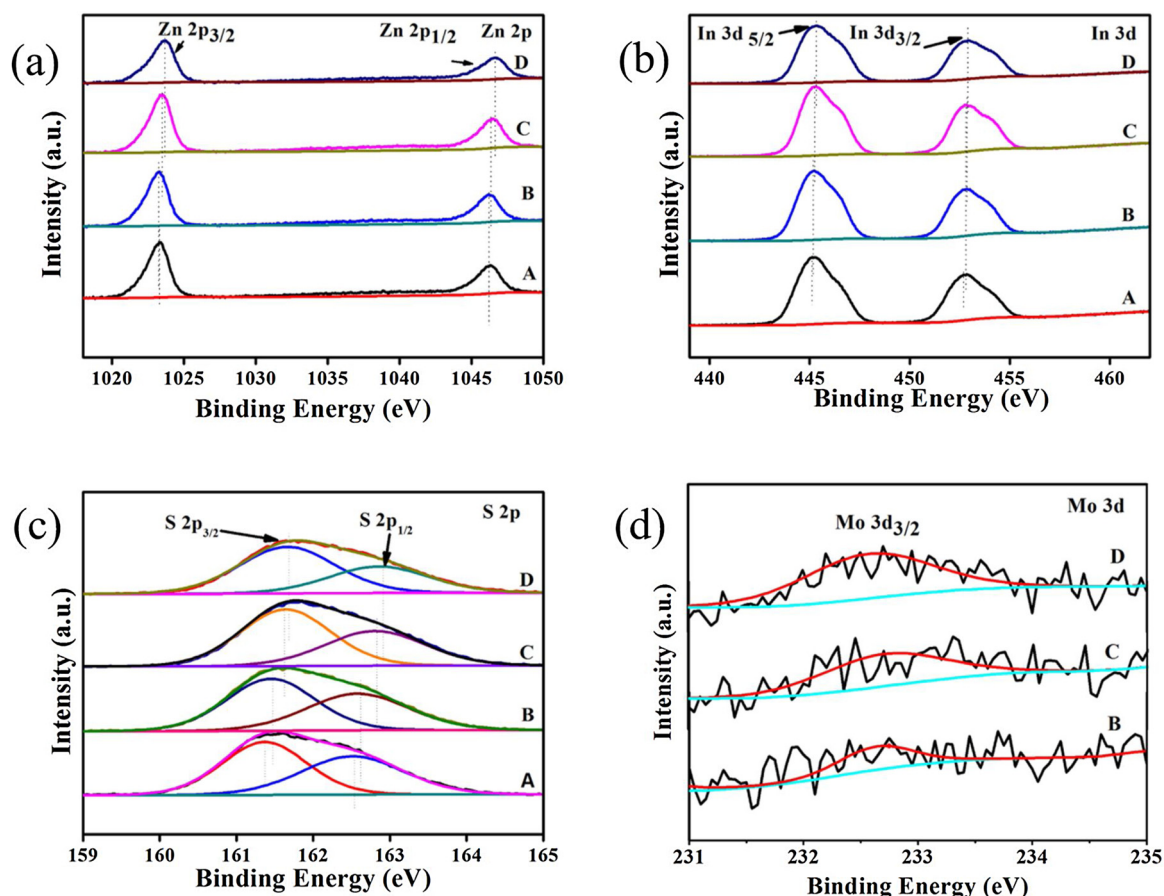


Fig. 5. XPS spectra of Zn 2p (a), In 3d (b), S 2p (c) and Mo 3d (d) for sample of ZnIn<sub>2</sub>S<sub>4</sub> (A), 3%-MoS<sub>2</sub>/ZnIn<sub>2</sub>S<sub>4</sub> (B) 5%-MoS<sub>2</sub>/ZnIn<sub>2</sub>S<sub>4</sub> (C) and 8%-MoS<sub>2</sub>/ZnIn<sub>2</sub>S<sub>4</sub> (D).

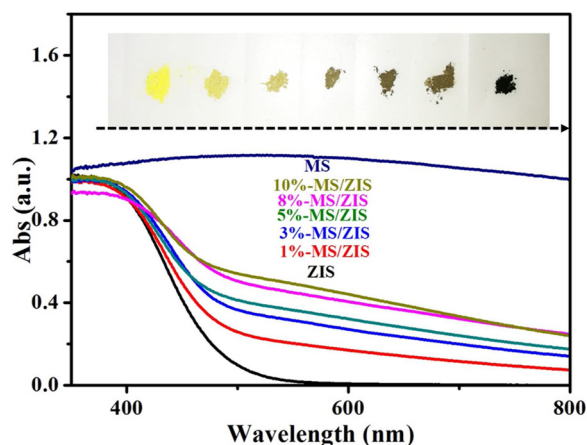


Fig. 6. The UV-vis diffuse reflectance spectrum of the pure ZnIn<sub>2</sub>S<sub>4</sub>, MoS<sub>2</sub> and MoS<sub>2</sub>/ZnIn<sub>2</sub>S<sub>4</sub> composite.

MoS<sub>2</sub>/ZnIn<sub>2</sub>S<sub>4</sub>, as shown in Fig. S2. With the increase of light wavelength, the photon-to-electron conversion efficiency of pure ZnIn<sub>2</sub>S<sub>4</sub> and MoS<sub>2</sub>/ZnIn<sub>2</sub>S<sub>4</sub> decreased, but the photoelectric conversion efficiency was enhanced by loading MoS<sub>2</sub> on ZnIn<sub>2</sub>S<sub>4</sub> as compared with the pure ZnIn<sub>2</sub>S<sub>4</sub>. Thus, MoS<sub>2</sub> could enhance the efficient utilization of the solar energy and the photocatalytic activity [49,50]. Many research works had been intensively verified the enhanced effect of MoS<sub>2</sub> [51]. Electrochemical impedance spectroscopy (EIS) was also conducted, as shown in Fig. 7b. The arc radius on the EIS Nyquist of pristine ZnIn<sub>2</sub>S<sub>4</sub> was bigger than the 5%-MoS<sub>2</sub>/ZnIn<sub>2</sub>S<sub>4</sub> composite. And the charge-transfer resistances (R<sub>ct</sub>) were obtained by fitting the curve of

Electrochemical impedance spectroscopy (EIS), as shown in Fig. S3. The R<sub>ct</sub> of 5%-MoS<sub>2</sub>/ZnIn<sub>2</sub>S<sub>4</sub> was 265 Ω, which is lower than that of the pristine ZnIn<sub>2</sub>S<sub>4</sub> (2900 Ω). This confirmed the enhanced effect of MoS<sub>2</sub> on the separation of photoinduced charge carriers [49]. The photoluminescence (PL) emission spectra were conducted to investigate the transfer efficiency of the interfacial electron from ZnIn<sub>2</sub>S<sub>4</sub> to MoS<sub>2</sub>. In Fig. 7c, the 5%-MoS<sub>2</sub>/ZnIn<sub>2</sub>S<sub>4</sub> composite showed lower PL peak than that of the pure ZnIn<sub>2</sub>S<sub>4</sub>. It is commonly known that the PL result represents the recombination rate of free electrons and holes. The stronger PL intensity, the greater is the recombination probability of photogenerated carriers. The time-resolved fluorescence decay of the pristine ZnIn<sub>2</sub>S<sub>4</sub> and the 5%-MoS<sub>2</sub>/ZnIn<sub>2</sub>S<sub>4</sub> was detected as shown in the Fig. S4. The fluorescence life time of the 5%-MoS<sub>2</sub>/ZnIn<sub>2</sub>S<sub>4</sub> was 3.96 ns longer than the ZnIn<sub>2</sub>S<sub>4</sub> (2.89 ns). The results demonstrated that the MoS<sub>2</sub> exhibited the photogenerated electron-hole recombination of ZnIn<sub>2</sub>S<sub>4</sub> [52]. Therefore, the introduction of MoS<sub>2</sub> greatly reduced the recombination probability of charge carriers on ZnIn<sub>2</sub>S<sub>4</sub>. The formation of heterostructure between MoS<sub>2</sub> and ZnIn<sub>2</sub>S<sub>4</sub> can effectively speed up separation and transfer of the photogenerated electron-hole pairs of composite and thus prevented the recombination of electron-hole pairs, which can strengthen the utilization of electronics for photocatalytic hydrogen evolution.

### 3.2. Photocatalytic H<sub>2</sub> evolution activity

The experimental measurements of photocatalytic H<sub>2</sub> production were carried out in a closed reaction system. Visible light (λ ≥ 420 nm) was used as light source and Na<sub>2</sub>S/Na<sub>2</sub>SO<sub>3</sub> solutions were used as sacrificial agents. As shown in Fig. 8a, little H<sub>2</sub> production was detected in the reaction system using the individual MoS<sub>2</sub> and ZnIn<sub>2</sub>S<sub>4</sub> (11 μmol g<sup>-1</sup> h<sup>-1</sup>) as photocatalysts. However, when MoS<sub>2</sub> was

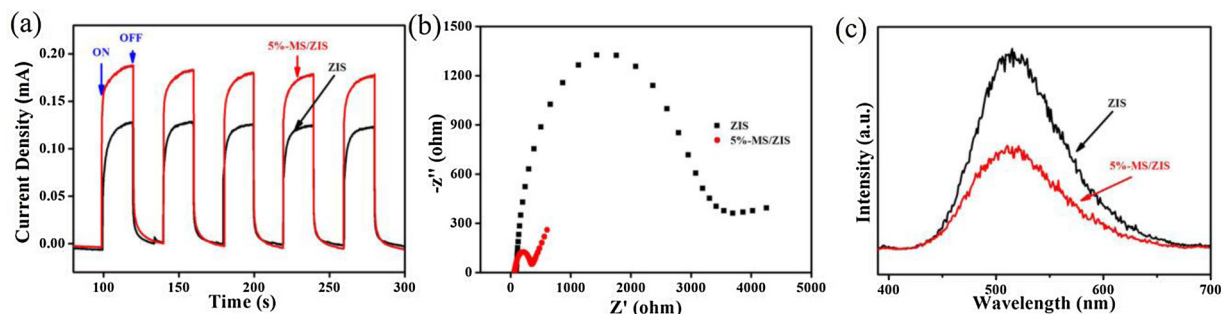


Fig. 7. The visible light photocurrent response of the pristine ZnIn<sub>2</sub>S<sub>4</sub> and 5%-MoS<sub>2</sub>/ZnIn<sub>2</sub>S<sub>4</sub> composite in 0.2 M Na<sub>2</sub>SO<sub>4</sub> aqueous solution under visible light irradiation (a); the EIS Nyquist plots of the pristine ZnIn<sub>2</sub>S<sub>4</sub> and 5%-MoS<sub>2</sub>/ZnIn<sub>2</sub>S<sub>4</sub> composite (b); room-temperature PL of the pristine ZnIn<sub>2</sub>S<sub>4</sub> and 5%-MoS<sub>2</sub>/ZnIn<sub>2</sub>S<sub>4</sub> composite (excited at 365 nm).

hybridized with ZnIn<sub>2</sub>S<sub>4</sub>, the H<sub>2</sub> production was achieved a great improvement under the same experimental conditions and dependent on the MoS<sub>2</sub> contents. 1%-MoS<sub>2</sub> hybrid increases the hydrogen production rate to 363.8  $\mu\text{mol g}^{-1} \text{h}^{-1}$ . Further increasing to 5%-MoS<sub>2</sub> hybrid, the activity of hydrogen production was reached to maximum rate of 3891.6  $\mu\text{mol g}^{-1} \text{h}^{-1}$ , which was 381 times higher than the pure ZnIn<sub>2</sub>S<sub>4</sub>. However, when the content of MoS<sub>2</sub> exceeded 5%, the H<sub>2</sub> production rate started to go down as 1368.9  $\mu\text{mol g}^{-1} \text{h}^{-1}$  for 8%-MoS<sub>2</sub>/ZnIn<sub>2</sub>S<sub>4</sub> and 431.6  $\mu\text{mol g}^{-1} \text{h}^{-1}$  for 10%-MoS<sub>2</sub>/ZnIn<sub>2</sub>S<sub>4</sub>. The reason for this result may be that the introduction of excess MoS<sub>2</sub> may override the active sites on ZnIn<sub>2</sub>S<sub>4</sub>, leading to a reduction in the activity of hydrogen production. It was worth mentioning that when we used 1% or 5% Pt loaded ZnIn<sub>2</sub>S<sub>4</sub> as photocatalysts for comparison, the hydrogen production rates were respectively 2815.7 or 1421.7  $\mu\text{mol g}^{-1} \text{h}^{-1}$ , which were lower than the optimal 5%-MoS<sub>2</sub>/ZnIn<sub>2</sub>S<sub>4</sub> of 3891.6  $\mu\text{mol g}^{-1} \text{h}^{-1}$ . These results proved that MoS<sub>2</sub> was a very effective hybrid for promoting photocatalytic H<sub>2</sub> evolution as compared with the noble metal Pt, although Pt was the most efficient cocatalyst to modify the semiconductor functional materials for maximizing the efficiency of photocatalytic H<sub>2</sub> evolution reactions [39]. Moreover, the prepared MoS<sub>2</sub>/ZnIn<sub>2</sub>S<sub>4</sub> heterostructures display a better photocatalytic activity of hydrogen evolution as compared with the reported MoS<sub>2</sub>/ZnIn<sub>2</sub>S<sub>4</sub> heterostructure photocatalyst synthesized through conventional methods under the similar conditions [42,43–46], as listed in Table S2. In Fig. 8b, the hydrogen production of 5%-MoS<sub>2</sub>/ZnIn<sub>2</sub>S<sub>4</sub> composite samples was compared with the mechanically mixed the corresponding amount of MoS<sub>2</sub> and ZnIn<sub>2</sub>S<sub>4</sub>. The results showed that the hydrogen production rate of the mechanical mixing of the samples was 408.8  $\mu\text{mol g}^{-1} \text{h}^{-1}$ , which was far smaller than that of the corresponding MoS<sub>2</sub>/ZnIn<sub>2</sub>S<sub>4</sub> composite. This suggests that the formation of heterojunction between MoS<sub>2</sub> and ZnIn<sub>2</sub>S<sub>4</sub> can

effectively promote the separation of photogenerated charge carriers.

The activity stability of the catalyst is also very significant important. In order to detect the stability, 5%-MoS<sub>2</sub>/ZnIn<sub>2</sub>S<sub>4</sub> under visible light irradiation was performed in the time dependent photocatalytic hydrogen production cycle experiment, as shown in Fig. 9a. A total of three cycles with each period of four hours were carried out. Hydrogen production activity of 5%-MoS<sub>2</sub>/ZnIn<sub>2</sub>S<sub>4</sub> did not decrease significantly at the second cycle. However, when the reaction was prolonged to the third round, the catalytic activity of hydrogen production was reduced to a certain extent with the hydrogen production rate decreased to 2674.9  $\mu\text{mol g}^{-1} \text{h}^{-1}$ . This suggests that light corrosion occurred in MoS<sub>2</sub>/ZnIn<sub>2</sub>S<sub>4</sub> composite during the prolonging reaction processes. The wavelength dependence of the photocatalytic activity of H<sub>2</sub> evolution was also examined with band-pass filters of different wavelengths, as shown in Fig. 9b. Hydrogen production efficiency decreased with the increasing of incident wavelength. Under  $\lambda = 420 \text{ nm}$  wavelength light illumination, the rate of H<sub>2</sub> production got to 565.4  $\mu\text{mol g}^{-1} \text{h}^{-1}$ . When the wavelength light was shifted to  $\lambda = 450 \text{ nm}$ , the hydrogen production rate is reduced to 112  $\mu\text{mol g}^{-1} \text{h}^{-1}$ . H<sub>2</sub> cannot be detected under 500 nm light illumination. It should be noted that the trends of H<sub>2</sub> yields with different wavelengths was significant deviation from the optical absorption of MoS<sub>2</sub>/ZnIn<sub>2</sub>S<sub>4</sub> composites, but closely agreed with the optical absorption of the pure ZnIn<sub>2</sub>S<sub>4</sub>. This suggests that the ZnIn<sub>2</sub>S<sub>4</sub> is acted as the real photoexcited center in the composited catalyst for driving photocatalytic hydrogen evolution.

Based on the above study and experimental results, the possible reaction process of photocatalytic hydrogen production over the MoS<sub>2</sub>/ZnIn<sub>2</sub>S<sub>4</sub> composite catalyst is proposed in Scheme 1. Under visible light illumination of MoS<sub>2</sub>/ZnIn<sub>2</sub>S<sub>4</sub> heterostructure, ZnIn<sub>2</sub>S<sub>4</sub> was excited to produce electrons on the conduction band (CB), and the holes stayed on the valence band (VB). The flat band potentials of ZnIn<sub>2</sub>S<sub>4</sub> can be

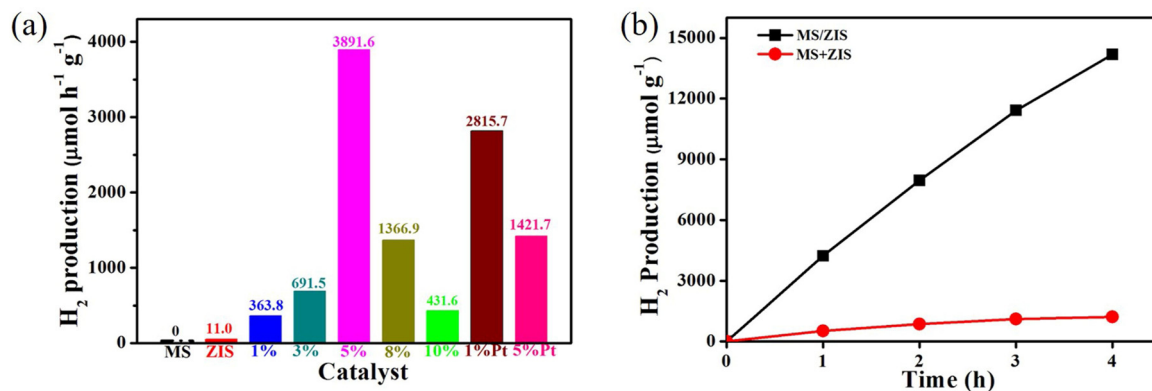


Fig. 8. The result of H<sub>2</sub> production of the pure MoS<sub>2</sub>, ZnIn<sub>2</sub>S<sub>4</sub>, and ZnIn<sub>2</sub>S<sub>4</sub> loaded with different cocatalysts (1%-MoS<sub>2</sub>/ZnIn<sub>2</sub>S<sub>4</sub>, 3%-MoS<sub>2</sub>/ZnIn<sub>2</sub>S<sub>4</sub>, 5%-MoS<sub>2</sub>/ZnIn<sub>2</sub>S<sub>4</sub>, 8%-MoS<sub>2</sub>/ZnIn<sub>2</sub>S<sub>4</sub>, 10%-MoS<sub>2</sub>/ZnIn<sub>2</sub>S<sub>4</sub>, 1%-Pt/ZnIn<sub>2</sub>S<sub>4</sub> and 5%-Pt/ZnIn<sub>2</sub>S<sub>4</sub>) (a); Evolution of H<sub>2</sub> over the 5%-MoS<sub>2</sub>/ZnIn<sub>2</sub>S<sub>4</sub> composite and 5%-MoS<sub>2</sub> + ZnIn<sub>2</sub>S<sub>4</sub> samples blending on the machine (b).



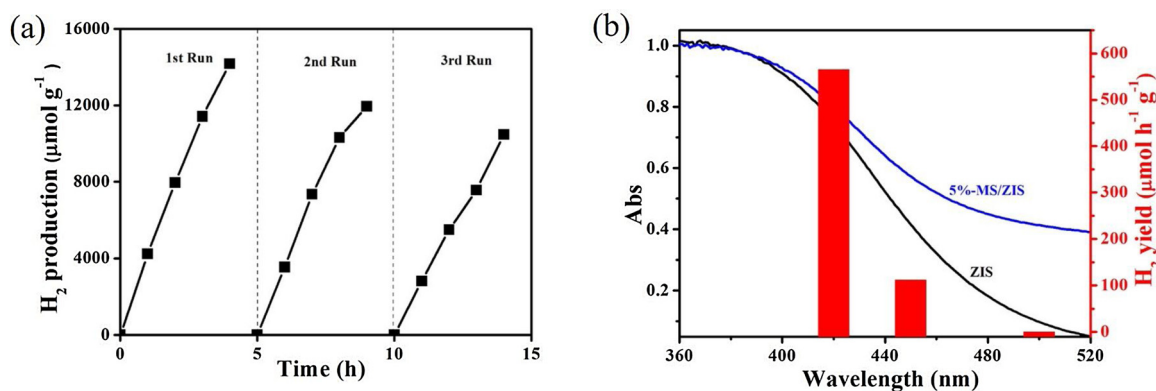
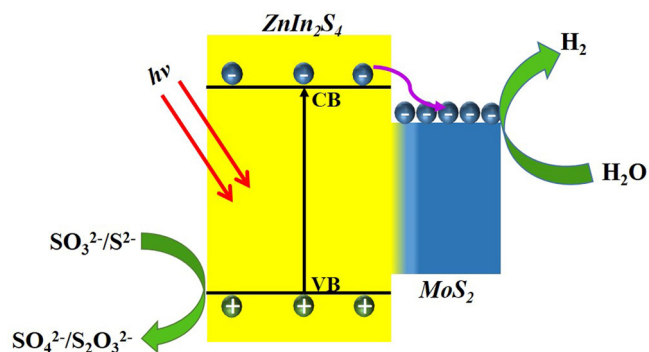


Fig. 9. Cyclic H<sub>2</sub> production on 5%-MoS<sub>2</sub>/ZnIn<sub>2</sub>S<sub>4</sub> (a); DRS patterns of the 5%-MoS<sub>2</sub>/ZnIn<sub>2</sub>S<sub>4</sub> samples and the rate of H<sub>2</sub> evolution of the 5%-MoS<sub>2</sub>/ZnIn<sub>2</sub>S<sub>4</sub> under  $\lambda = 420$  nm, 450 nm and 500 nm light (b).



Scheme 1. Possible schematic mechanism of MoS<sub>2</sub>/ZnIn<sub>2</sub>S<sub>4</sub> composite for photocatalytic hydrogen evolution.

determined by Mott–Schottky measurements (Fig. S5a) and were found to be  $-0.84$  V (vs. NHE) [53], which is equal to the CB position of ZnIn<sub>2</sub>S<sub>4</sub>. The bandgap energy of the pure ZnIn<sub>2</sub>S<sub>4</sub> was estimated to be 2.28 eV by extrapolating the linear part of  $(\alpha h\nu)^{1/2}$  vs. photon energy (Fig. S5b) [51]. The position of the valence band of ZnIn<sub>2</sub>S<sub>4</sub> was calculated to be 1.44 V according to the formula  $E_{VB} = E_{CB} + E_g$ . This result is basically consistent with the theoretical value [54,55]. The CB position of ZnIn<sub>2</sub>S<sub>4</sub> was more negative than the corresponding level of MoS<sub>2</sub> ( $-0.5$  eV), the transfer of photogenerated electrons from the ZnIn<sub>2</sub>S<sub>4</sub> to MoS<sub>2</sub> through heterostructure interface was beneficial in thermodynamics. MoS<sub>2</sub> was acted as a trap site of photogenerated electrons to suppress the combination of the photogenerated carriers. The electrons on MoS<sub>2</sub> will reduce H<sub>2</sub>O into H<sub>2</sub> evolution. Meanwhile, the holes on the ZnIn<sub>2</sub>S<sub>4</sub> valence band were consumed by the sacrificial agent in the solution. The subtle atomic-level intimate contact and strong interactions between ZnIn<sub>2</sub>S<sub>4</sub> and MoS<sub>2</sub> were crucial for inter-electron transfer between the two components and thus a highly efficient photocatalytic activity.

#### 4. Conclusions

The intimate contact MoS<sub>2</sub>/ZnIn<sub>2</sub>S<sub>4</sub> heterostructure photocatalysts were in-situ synthesized by a one-pot solvothermal reaction. The as-prepared MoS<sub>2</sub>/ZnIn<sub>2</sub>S<sub>4</sub> composites exhibited a nearly uniform size of flower-like microsphere morphology assembled by the thin nanosheets. The MoS<sub>2</sub>/ZnIn<sub>2</sub>S<sub>4</sub> heterostructure photocatalysts greatly improve the photocatalytic performance of ZnIn<sub>2</sub>S<sub>4</sub> for H<sub>2</sub> evolution under visible light illumination. The hydrogen production activity reaches 3891.6  $\mu\text{mol g}^{-1} \text{h}^{-1}$  in the optimal 5%-MoS<sub>2</sub>/ZnIn<sub>2</sub>S<sub>4</sub> system, which exceeded the photocatalytic activity of 1%-Pt/ZnIn<sub>2</sub>S<sub>4</sub>. The subtle atomic-level intimate contact and strong interactions between ZnIn<sub>2</sub>S<sub>4</sub> and MoS<sub>2</sub> in MoS<sub>2</sub>/ZnIn<sub>2</sub>S<sub>4</sub> contributed to a highly efficient

interelectron transfer between the two components and thus photocatalytic activity. These results provide inspiration for the design of composited photocatalysts with efficient photocatalytic H<sub>2</sub> evolution.

#### Acknowledgments

This work is financially supported by the National Natural Science Foundation of China (Grants Nos. 21673042 and 21673043), and the Natural Science Foundation of Fujian Province of PR China (2017J01411), and the Technology Project of Education Office of Fujian Province of PR China (JAT160045).

#### Appendix A. Supplementary data

Supplementary material related to this article can be found, in the online version, at doi:<https://doi.org/10.1016/j.apcatb.2018.04.006>.

#### References

- [1] X. Chen, S. Shen, L. Guo, S.S. Mao, Chem. Rev. 110 (2010) 6503–6570.
- [2] X. Bu, P. Wu, Y.W. Zhou, Angew. Chem. Int. Ed. 56 (2017) 13001–13005.
- [3] J. Li, B. Du, Z. Lu, Q. Meng, J. Sha, New J. Chem. 41 (2017) 10966–10971.
- [4] Z. Shi, Y. Wang, H. Lin, H. Zhang, M. Shen, S. Xie, Y. Zhang, Q. Gao, Y. Tang, J. Mater. Chem. A 4 (2016) 6006–6013.
- [5] L. Stegbauer, K. Schwinghammer, B.V. Lotsch, Chem. Sci. 5 (2014) 2789–2793.
- [6] V.S. Vyas, F. Haase, L. Stegbauer, G. Savasci, F. Podjaski, C. Ochsenfeld, B.V. Lotsch, Nat. Commun. 6 (2015) 8508–8516.
- [7] F. Haase, T. Banerjee, G. Savasci, C. Ochsenfeld, B.V. Lotsch, Faraday Discuss. 201 (2017) 247–264.
- [8] J. Zhang, Y. Wang, J. Jin, J. Zhang, Z. Lin, F. Huang, J. Yu, ACS Appl. Mater. Interfaces 5 (2013) 10317–10324.
- [9] S. Duan, G. Han, Y. Su, X. Zhang, Y. Liu, X. Wu, B. Li, Langmuir 32 (2016) 6272.
- [10] L. Ge, F. Zuo, J. Liu, Q. Ma, C. Wang, D. Sun, L. Bartels, P. Feng, J. Phys. Chem. C 116 (2012) 13708–13714.
- [11] S. Min, G. Lu, J. Phys. Chem. C 116 (2012) 19644–19652.
- [12] Q. Zhang, L. Gao, Langmuir 20 (2004) 9821–9827.
- [13] R. Abe, M. Higashi, K. Domen, J. Am. Chem. Soc. 132 (2010) 11828–11829.
- [14] Q. Li, B. Guo, J. Yu, J. Ran, B. Zhang, H. Yan, J.R. Gong, J. Am. Chem. Soc. 133 (2011) 10878–10884.
- [15] V.M. Daskalaki, M. Antoniadou, G.L. Puma, D.I. Kondarides, P. Lianos, Environ. Sci. Technol. 44 (2010) 7200–7205.
- [16] X. Wang, G. Liu, G.Q. Lu, H.M. Cheng, Int. J. Hydrogen Energy 35 (2010) 8199–8205.
- [17] Y.J. Zhang, W. Yan, Y.P. Wu, Z.H. Wang, Mater. Lett. 62 (2008) 3846–3848.
- [18] L.H. Yao, D. Wei, Y.M. Ni, Nano Energy 26 (2016) 248–256.
- [19] L.H. Yao, N. Zhang, D.P. Yan, J. Power Sources 374 (2018) 142–148.
- [20] L.H. Yao, D. Wei, D.P. Yan, Chem. Asian J. 10 (2015) 630–636.
- [21] J. Kiwi, M. Grätzel, Nature 281 (1979) 657–658.
- [22] L.S. Yoong, F.K. Chong, B.K. Dutta, Energy 34 (2009) 1652–1661.
- [23] Y. Li, Y. Hu, S. Peng, G. Lu, S. Li, J. Phys. Chem. C 113 (2009) 9352–9358.
- [24] Y. Li, G. Chen, C. Zhou, J. Sun, Chem. Commun. (2009) 2020–2022.
- [25] S.R. Kadam, R.P. Panmand, R.S. Sonawane, S.W. Gosavi, B.B. Kale, RSC Adv. 5 (2015) 58485–58490.
- [26] Q. Wang, N. An, Y. Bai, H. Hang, J. Li, X. Lu, Y. Liu, F. Wang, Z. Li, Z. Lei, Int. J. Hydrogen Energy 38 (2013) 10739–10745.
- [27] X. Tang, Q. Tay, Z. Chen, Y. Chen, G.K.L. Goh, J. Xue, New J. Chem. 37 (2013) 1878–1882.

- [28] I. Tsuji, Y. Shimodaira, H. Kato, H. Kobayashi, A. Kudo, *Chem. Mater.* 22 (2010) 1402–1409.
- [29] J. Ding, S. Sun, W. Yan, J. Bao, C. Gao, *Int. J. Hydrogen Energy* 38 (2013) 13153–13158.
- [30] Y. Yu, G. Chen, G. Wang, Z. Lv, *Int. J. Hydrogen Energy* 38 (2013) 1278–1285.
- [31] H. He, J. Lin, W. Fu, X. Wang, H. Wang, Q. Zeng, Q. Gu, Y. Li, C. Yan, B.K. Tay, *Adv. Energy Mater.* 6 (2016) 1600464–1600470.
- [32] Y.J. Yuan, F. Wang, B. Hu, H.W. Zu, Z.T. Yu, Z.G. Zou, *Dalton Trans.* 44 (2015) 10997–11003.
- [33] W.H. Yuan, Z.L. Xia, L. Li, *Chin. Chem. Lett.* 24 (2013) 984–986.
- [34] J. Hou, C. Yang, H. Chen, Z. Wang, S. Jiao, H. Zhu, *Phys. Chem. Chem. Phys.: PCCP* 15 (2013) 15660–15668.
- [35] Y. Li, J. Wang, S. Peng, G. Lu, S. Li, *Int. J. Hydrogen Energy* 35 (2010) 7116–7126.
- [36] X. Zong, G. Wu, H. Yan, G. Ma, J. Shi, F. Wen, L. Wang, C. Li, *J. Phys. Chem. C* 114 (2010) 1963–1968.
- [37] L. Wei, Y. Chen, J. Zhao, Z. Li, *Beilstein J. Nanotechnol.* 4 (2013) 949–955.
- [38] D. Zeng, L. Xiao, W.J. Ong, P. Wu, H. Zheng, Y. Chen, *ChemSusChem* 10 (2017) 4624–4631.
- [39] Y. Li, K. Zhang, S. Peng, G. Lu, S. Li, *J. Mol. Catal. A: Chem.* 363–364 (2012) 354–361.
- [40] Q. Xiang, J. Yu, M. Jaroniec, *J. Am. Chem. Soc.* 134 (2012) 6575–6578.
- [41] W. Zhou, Z. Yin, Y. Du, X. Huang, Z. Zeng, Z. Fan, H. Liu, J. Wang, H. Zhang, *Small* 9 (2013) 140–147.
- [42] L. Wei, Y. Chen, Y. Lin, H. Wu, R. Yuan, Z. Li, *Appl. Catal. B: Environ.* 144 (2014) 521–527.
- [43] G.P. Chen, N. Ding, F. Li, Y.Z. Fan, Y.H. Luo, D.M. Li, Q.B. Meng, *Appl. Catal. B: Environ.* 160–161 (2014) 614–620.
- [44] Y.J. Yuan, J.R. Tu, Z.J. Ye, *Appl. Catal. B: Environ.* 188 (2016) 13–22.
- [45] L. Wei, Y.J. Chen, J.L. Zhao, Z.H. Li, *Beilstein J. Nanotechnol.* 4 (2013) 949–955.
- [46] H. Liu, J. Zhang, D. Ao, *Appl. Catal. B: Environ.* 221 (2018) 433–442.
- [47] Z. Chen, J. Xu, Z. Ren, Y. He, G. Xiao, *J. Solid State Chem.* 205 (2013) 134–141.
- [48] J. Chen, S.H. Shen, P.H. Guo, M. Wang, *Appl. Catal. B: Environ.* 152–153 (2014) 335–341.
- [49] Y.Q. Tang, R.R. Wang, Y. Yang, D.P. Yan, X. Xiang, *ACS Appl. Mater. Int.* 8 (2016) 19446–19455.
- [50] Y.Q. Tang, W.H. He, L. Lu, J. Fielden, *J. Phys. Chem. C* 118 (2014) 25365–25373.
- [51] W. Li, L. Zhang, G. Yang, *Nanoscale* 9 (2017) 18290–18298.
- [52] Q.H. Liang, Z. Li, Z.H. Huang, F.Y. Kang, Q.H. Yang, *Adv. Funct. Mater.* 25 (2015) 6885–6892.
- [53] H.S. Park, K.E. Kweon, H. Ye, E. Paek, G.S. Hwang, A.J. Bard, *J. Phys. Chem. C* 115 (2011) 17870–17879.
- [54] W.Y. Lim, M. Hong, G.W. Ho, *Dalton Trans.* 45 (2016) 552–560.
- [55] Y. Zhang, S. Dian, *CrystEngComm.* 13 (2011) 4770–4776.